Journal of Power Sources 209 (2012) 120–129

Contents lists available at SciVerse ScienceDirect

Journal of Power Sources

journal homepage: www.elsevier.com/locate/jpowsour

Cr-poisoning of a $LaNi_{0.6}Fe_{0.4}O_3$ cathode under current load

M.K. Stodolny[a,*], B.A. Boukamp[b], D.H.A. Blank[b], F.P.F. van Berkel[a]

[a] Energy Research Centre of the Netherlands (ECN), Hydrogen and Clean Fossil Fuels, P.O. Box 1, 1755 ZG, Petten, The Netherlands
[b] Department of Science and Technology & MESA+ Institute for Nanotechnology, University of Twente, 7500 AE, Enschede, The Netherlands

ARTICLE INFO

Article history:
Received 20 January 2012
Received in revised form 10 February 2012
Accepted 21 February 2012
Available online 1 March 2012

Keywords:
SOFC cathode
Cr-poisoning
Cr vapor transport
LNF
SOFC interconnect
GDC barrier layer

ABSTRACT

This study demonstrates the significant impact of Cr-poisoning on the performance of the $LaNi_{0.6}Fe_{0.4}O_3$ (LNF) SOFC cathode under current load. Volatile Cr-species, originating from a porous metallic foam, enter the working electrode and modify both the LNF cathode layer and the $Gd_{0.4}Ce_{0.6}O_{1.8}$ (GDC) barrier layer, causing increasing overpotential and cell impedance. The increase of the ohmic resistance is caused by a decrease of the in-plane electronic conductivity of the LNF layer (due to Cr incorporation and Ni removal from the LNF perovskite lattice) combined with a deterioration of the ionic conductivity of the GDC barrier layer due to reactivity with Cr resulting in formation of a $GdCrO_3$-phase. The increase of the polarisation resistance is caused by a decrease of the electrochemical activity of the LNF surface towards oxygen reduction reaction at the triple phase boundary (TPB) due to Cr-incorporation in the outer shell of the LNF grains. Chemical reaction and electrochemically driven reaction of volatile Cr-species with LNF and GDC contributes to the extrinsic degradation of the LNF cathodes under current load.

1. Introduction

The perovskite $LaNi_{0.6}Fe_{0.4}O_3$ (LNF) has been considered as a candidate cathode and interconnect coating material for various intermediate temperature SOFC (IT-SOFC) systems where relatively cheap interconnect materials such as chromia-forming ferritic stainless steels are used. High electronic conductivity and a thermal expansion coefficient matching that of zirconia [1], together with claimed high Cr-resistance [2–4] are the properties of LNF that enable its use as current collecting layer, interconnect protective coating and/or electrochemically active cathode layer. In the context of Cr-tolerance, LNF has a claimed advantage of not being composed of the so-called Cr-nucleating-agents [5], like Mn^{2+} or SrO, which are inducing Cr-deposition (as reported for LSM or LSCF cathodes [5–7]).

However, previous studies regarding the actual Cr tolerance of LNF have demonstrated the occurrence of solid state reactivity of LNF with chromia at 800 °C [8,9]. It has also been found that volatile Cr species directly react with a porous LNF layer at IT-SOFC operating temperatures [10,11]: this reaction results in a replacement of Ni by Cr in the LNF perovskite lattice. One of the observed consequences of this replacement of Ni by Cr is a decrease of the in-plane electronic conductivity of the LNF porous layer [11].

In the present study the impact of volatile Cr species on the electrochemical properties of a $LaNi_{0.6}Fe_{0.4}O_3$ cathode has been investigated under current load, aiming for an evaluation of the reliability of a LNF cathode operating in a Cr-containing environment, such as in an IT-SOFC stack. To accelerate the Cr-poisoning impact, a Cr-containing porous interconnect foam has been used, which is distinctively different from a dense interconnect alloy employed in a real stack situation.

In order to unambiguously observe the degradation of the Cr-exposed LNF cathode under electrochemical operation, a special set-up was required. Reliable three-electrode measurements, facilitating a square planar geometry with coplanar reference electrodes, allowed insight into the cathode degradation under stationary conditions (400 mA cm^{-2} at 800 °C). Changes in the overpotential and the evolution of the electrochemical impedance spectra of the working LNF electrode were monitored over a time period of 1000 h. The accuracy of the three-electrode measurements has been assured by virtually perfect electrodes alignment, obtained with precise laser-ablation trimming of the edges of the electrodes.

Based on the analysis of the electrochemical impedance and electronic conductivity measurements, together with detailed post-mortem analyses on the Cr-exposed sample, a mechanism is proposed for the Cr-poisoning of $LaNi_{0.6}Fe_{0.4}O_3$ cathodes under current load.

2. Experimental

2.1. Sample preparation

LNF cathode layers were prepared using a commercial $LaNi_{0.6}Fe_{0.4}O_3$ powder (Praxair, 99.9% purity). A 3 mol% yttria stabilized zirconia (YSZ) electrolyte, providing the mechanical

* Corresponding author. Tel.: +31 224 564074; fax: +31 224 568489.
E-mail addresses: maciej.stodolny@gmail.com, stodolny@ecn.nl (M.K. Stodolny).

0378-7753/$ – see front matter © 2012 Elsevier B.V. All rights reserved.
doi:10.1016/j.jpowsour.2012.02.083

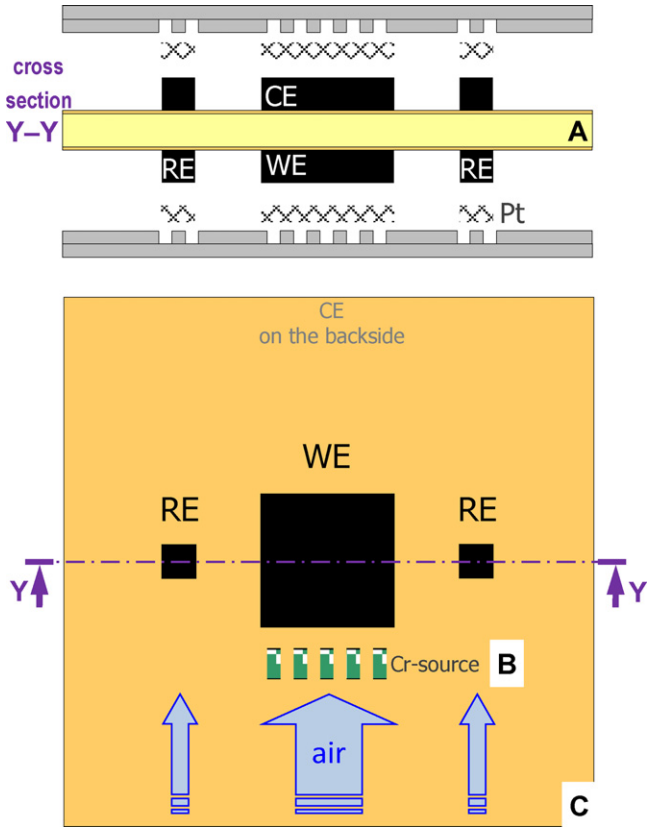

Fig. 1. Endurance testing of the LNF cathode as the working electrode (WE) was performed in a 'three-electrode set-up' (A) for a Cr-free case and with a Cr-source added (B). A square planar geometry with coplanar reference electrodes (RE) was used (C).

support, was prepared by tape casting and sintering at 1500 °C for 1 h. The electrolyte squares, with dimensions 80 mm × 80 mm and 150 μm thickness, were subsequently covered on both sides with 2 μm thick $Gd_{0.4}Ce_{0.6}O_{1.8}$ (GDC) barrier layers by means of screen printing, followed by sintering at 1300 °C for 1 h. The LNF powder, after precalcination at 800 °C for 1 h in air, was milled and dispersed into an alcohol-binder solution using a Dispermat (VMA-Getzmann GmbH) milling system. The LNF paste was screen printed on top of the GDC barrier layer on both sides of the electrolyte in a pattern shown in Fig. 1.

A perfectly aligned working electrode (WE) and counter electrode (CE), vital for a coplanar reference electrode geometry [12–16], was successfully obtained by laser aided trimming of the electrode edges. A special chuck (sample holder/clamp) was designed to precisely reverse the electrolyte providing a high spatial accuracy of the laser trimming on both sides of the sample. Dried, but not sintered, LNF layers were trimmed with the third harmonic of Nd:YAG laser (355 nm) (Rofin-Baasel). A groove of 60 μm width and circa 40 μm depth was obtained by laser ablation. The surplus of LNF material outside the groove was removed from the electrolyte surface by scraping it off with a zirconia blade.

Finally, the aligned symmetrical cell was sintered at 1150 °C for 1 h. The resulting LNF perovskite layers, with a thickness of approximately 35 μm, formed 3.8 cm^2 WE and CE electrodes, and 0.6 cm^2 reference electrodes (RE) as shown schematically in Fig. 1. A total misalignment between both corresponding edges of the WE and CE was measured using an Apex Vision Measuring Machine (Mitutoyo QuickVisionPRO). The misalignment was smaller than 10 μm, which is below 7% of the electrolyte thickness. Hence, such a misalignment is lower than the allowed maximum of 10% of the electrolyte thickness for accurate electrochemical characterization [17].

2.2. Electrochemical measurements

In order to investigate the electrochemical behavior of the Cr-free and the Cr-exposed LNF working electrodes, samples were heated to the operating temperature of 800 °C. The heating was performed at a rate of 30 °C h^{-1} under a flow of dry synthetic air, composed of 20% O_2 (purity 99.6%, <7 ppmv H_2O, where ppmv denotes parts per million in volume) and 80% N_2 (purity 99.999%, <4 ppmv H_2O), at a total flow rate of 500 ml min^{-1} for both the WE and the CE sides. After reaching the operating temperature the WE was cathodically polarized under a constant current load of 400 mA cm^{-2}. Applying such a current load is in line with the standard testing procedure at ECN for a durability test at 800 °C. The current was applied using a Pt mesh. A Pt mesh was chosen instead of an Au mesh, which would have been the preferred choice for electrochemical inertness, because of reported reactivity of Au with metallic interconnects. Metallic interconnects were used as the Cr-source during the electrochemical characterization, as described hereafter. The load was interrupted approximately every 200 h for *I–V* measurements and impedance analysis at open circuit voltage (OCV), though the discussion of these results is beyond the scope of this paper. Voltage signal between the WE and both reference electrodes RE on both sides of the working electrode was continuously recorded and electrochemical impedance spectroscopy (EIS) was performed under load after periods of circa 200 h uninterrupted operation. EIS measurements were performed with a Solartron 1255 frequency response analyzer in conjunction with a Solartron 1287A electrochemical interface. The applied frequencies ranged from 100 kHz to 0.1 Hz with a signal amplitude of 10 mV.

The voltage signals between the WE and both reference electrodes (RE) were compared and averaged for each measurement point. For the Cr-free reference cell a nearly perfect match between both signals (WE–RE1 and WE–RE2) was observed over the entire operating time, demonstrating the effect of the aimed precision alignment of the WE and CE electrodes. For the Cr-poisoned cell initially an identically perfect match was observed, but an increasing imbalance between both WE–RE signals was observed over time. This is probably due to increasingly inhomogeneous poisoning over the working electrode as described in Section 4.1. In order to compensate for the imbalance, both WE–RE signals were averaged to obtain the overall electrochemical performance of the Cr-poisoned cell in terms of overpotential and cell impedance. The averaged voltage signal (WE–RE), representing electrode potential *E*, was corrected for the ohmic drop between WE and RE in order to present the true cathode overpotential value η. The correction was applied according to the relation: $\eta = E - i \cdot R_{ohmic}$, where i represents a current density and R_{ohmic} is the electrolyte contribution obtained from the EIS data under current load (as explained below).

Impedance data was fitted using the Eqcwin software [18–21] with an equivalent circuit of $R(RQ)(RQ)(RQ)$, where Q is a constant phase element and R represents various contributing resistances. Fitting of the EIS data provided values of the contributing resistances to the total resistance, i.e. ohmic (R_{ohmic}) and polarization resistance (R_{pol}).

The Cr-free sample was electrochemically operated in an all-ceramic housing. For the Cr-exposed sample an ITM-14 ferritic FeCr-based alloy in the form of a porous foam (Plansee AG, Reutte, Austria [22,23]) was used as the Cr source. The laser-cut foam was pre-oxidized for 100 h at 800 °C prior to the experiment to insure the presence of a Cr-containing oxide scale on the metal surface. The ITM-14 Cr-source was placed in the gas channels in front of the WE but without any direct contact neither with electrolyte nor

with WE. This allowed the air-flow to pick up volatile Cr species and transport them to the electrochemically operating WE, simulating the Cr evaporation from the stainless steel manifolds, metallic interconnects (MIC) and system components (BoP) of the IT-SOFC stack.

After completing the current load experiments the electrical in-plane conductivity was measured for both the Cr-free and the Cr-exposed working electrodes. For this a standard van der Pauw method was used at the operating temperature of 800 °C in air.

2.3. Post-mortem analyses

The elemental composition of the Cr-exposed LNF cathode layer was obtained at four different distances from the Cr-source. Therefore, four pieces were laser-cut along the direction of the gas flow. Subsequently, the CE electrode side was removed for each piece by polishing until YSZ electrolyte was reached and the remaining WE electrode was acid-dissolved and the elemental composition was measured by means of inductively coupled plasma-optical emission spectroscopy (ICP-OES), using a Varian Vista AX PRO CCD.

The embedded and polished cross-section of the Cr-exposed WE was analyzed by field emission scanning electron microscopy, using a Philips XL40-W SEM equipped with an Oxford Microspec 600 WDX (wavelength dispersive X-ray) detector.

For the cross-sectional transmission electron microscopy (TEM) study of the LNF/GDC/YSZ assembly of the Cr-exposed WE, a specimen was acquired using focused ion beam (FIB) lift-out sample preparation using a Nova 200 Nanolab SDB (small dual beam). TEM analyses were performed using an FEI Tecnai F30ST equipped with an EDAX energy dispersive X-ray (EDX) detector. All TEM experiments were performed at an acceleration voltage of 300 kV, using several modes of operation: Z-contrast imaging generated by high angle annular dark field (HAADF), general bright field TEM imaging (BF-TEM), energy dispersive X-ray analysis (EDX) in scanning TEM mode (STEM), and high resolution transmission electron microscopy (HRTEM) together with fast Fourier transform (FFT) analysis of the HRTEM images.

3. Degradation during operation conditions – results and discussion

3.1. Overpotential evolution in time

Fig. 2 shows the evolution of the WE cathode overpotential η measured versus the RE, and corrected for the ohmic drop between WE and RE, in Cr-free and in Cr-containing atmospheres at 800 °C under a load of 400 mA cm^{-2}. The reference Cr-free LNF cathode showed a stable overpotential over a testing period of 500 h. The LNF cathode exposed to volatile Cr species exhibited a relatively stable overpotential up to 200 h. After that a considerable increase in the overpotential losses was observed over a time period of approximately 200–1000 h.

During the initial 100 h the changes in the overpotential could be attributed to the so-called 'burn-in' process, characteristic for LNF cathodes [24].

For the reference LNF cathode tested in the all-ceramic housing no apparent degradation was observed over the full 500 h of operation. The Cr-containing atmosphere clearly caused a continuous and progressing degradation of the electrochemical performance of the LNF cathode tested over the period of 1000 h.

While the period of the current interruption had virtually no effect on the overpotential for the Cr-free cathode, a significant effect can be seen for the Cr-exposed cathode, especially after 400 h of operation (Fig. 2). After current switch off the WE relaxed

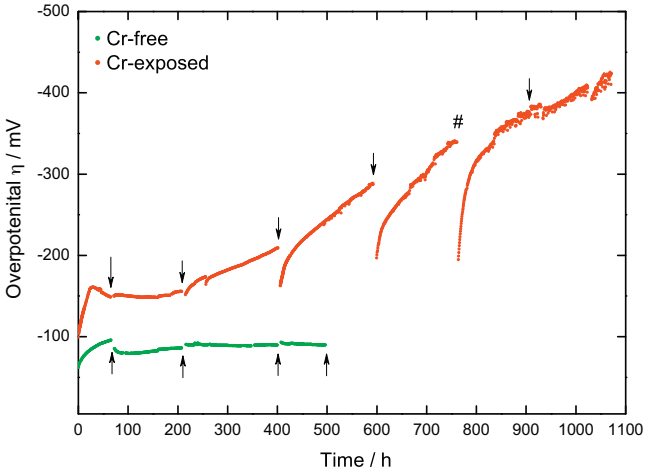

Fig. 2. Evolution of the cathode overpotential η with time for the LNF WE in Cr-free and in Cr-containing atmospheres. Arrows indicate the EIS measurements under load. A hash sign (#) depicts an accidental current interruption with no EIS measurements performed beforehand.

to a state with an initially significantly lower overpotential upon switching on the current. Similar transient recovery of the WE performance after a current interruption has been also observed for LSM cathode in the presence of Cr-based interconnect [25,26].

3.2. Evolution of the EIS

As indicated by the arrows in Fig. 2 the EIS was performed at the end of each uninterrupted operation period (about every 200 h) in order to follow the change in the electrochemical response of the LNF cathode under current load. Fig. 3 presents the electrochemical impedance evolution with time of the WE, averaged over both RE, measured under a load of 400 mA cm^{-2}. The reference Cr-free LNF cathode showed a stable and nearly constant impedance (Fig. 3A). The LNF cathode exposed to volatile Cr species

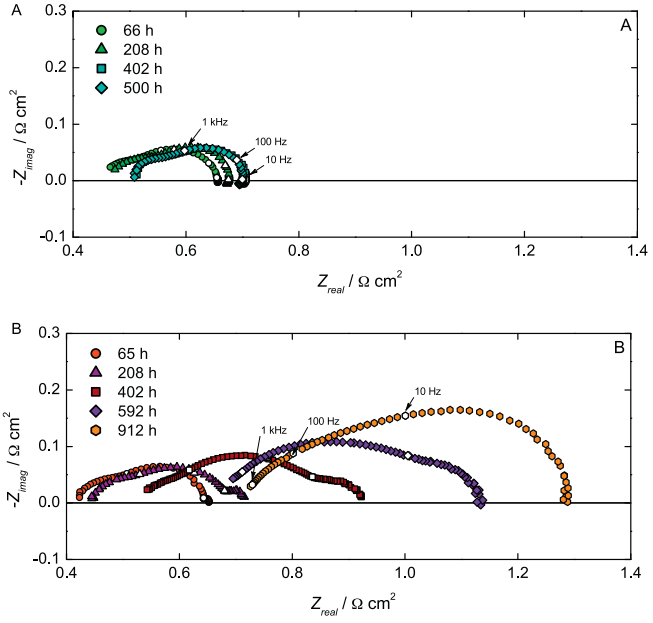

Fig. 3. Evolution of the WE impedance (EIS) with time, measured under a load of 400 mA cm^{-2} in Cr-free (A) and in Cr-containing atmospheres (B).

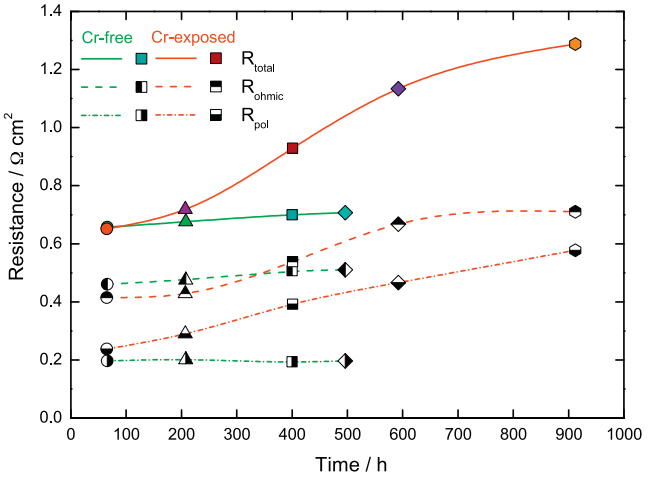

Fig. 4. Evolution of R_{total} and R_{ohmic} and R_{pol} in time at 400 mA cm^{-2} for Cr-free and Cr-exposed sample. Markers shape corresponds to markers in Fig. 3.

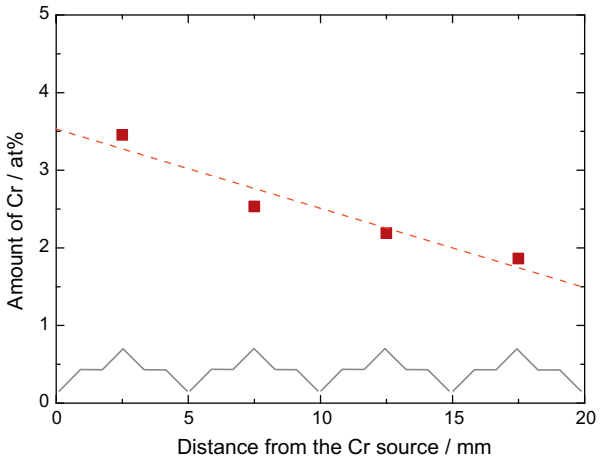

Fig. 5. The amount of Cr deposited in the Cr-exposed WE as a function of the distance from the Cr source. The concentration is given as La + Ni + Fe + Cr = 100 at.%. The brackets indicate schematically the regions of the ICP sampling.

exhibited relatively comparable EIS spectra up to 200 h, then a significant increase in size and shift to higher resistance values was observed for the impedance during the time period after 200 h (Fig. 3B).

3.2.1. Evolution of the contributing resistances obtained with EIS

Fig. 4 presents the evolution with time of the total (R_{total}), ohmic (R_{ohmic}) and polarization (R_{pol}) resistances of the tested LNF cathodes. The reference Cr-free cathode showed relatively stable values of both R_{ohmic} and R_{pol} resulting in a constant R_{total} during the testing period of 500 h. The LNF cathode exposed to volatile Cr species exhibited a continuous increase in R_{pol} throughout the experiment. R_{ohmic} was relatively stable up to 200 h, followed by a rather steep increase over the time period of circa 200–600 h, reaching a mild incline between 600 and 1000 h.

The LNF cathode tested in a Cr-free atmosphere showed stable values of both R_{ohmic} and R_{pol}, confirming the intrinsic stability of the LNF cathode under electrochemical operation. However, the LNF cathode tested in combination with a Cr-source showed clear deterioration of both R_{ohmic} and R_{pol} indicating extrinsic degradation due to Cr presence.

3.3. In-plane electronic conductivity of Cr-free and Cr-exposed sample

For both Cr-free and Cr-exposed samples, the in-plane electronic conductivity σ was measured at the operating temperature of 800 °C in order to determine the impact of volatile Cr-species on the electronic conductivity of the WE. The Cr-free LNF cathode layer showed an in-plane electronic conductivity of 204 S cm^{-1}. The Cr-exposed LNF cathode layer exhibited a lower electronic conductivity of 127 S cm^{-1}.

The in-plane electronic conductivity of the Cr-exposed LNF layer was lower than the electronic conductivity of the Cr-free layer which is in line with a previous study [10,11]. An increase in the in-plane resistance of the electrode can cause an apparent increase in R_{ohmic}. However, a drop in the conductivity of 77 S cm^{-1} (37%) does not explain the relatively large increase in R_{ohmic}. Other causes for the increase in R_{ohmic} were examined with the post-mortem analyses.

4. Post-mortem analyses – results and discussion

4.1. Overall Cr concentration in the Cr-exposed cathode as a function of the distance from the Cr source

Fig. 5 presents the overall Cr concentration as detected with the ICP-OES method for the Cr-exposed WE operated 1000 h at 800 °C under 400 mA cm^{-2} load. A preferential higher Cr accumulation was observed at the air inlet close to the Cr source. The Cr concentration decreased nearly linearly as a function of the distance from the Cr source.

Cr-EDX-mapping over the entire WE surface area (not shown) indicates a significant inhomogeneous Cr distribution along the gas flow direction ranging from ~3.5 at.% to ~1.5 at.%. This observed inhomogeneity would cause an imbalance between the respective WE-RE signals, as clearly has been observed for the Cr-poisoned electrode. For a better description of the overall performance of the electrode the WE-RE1 and WE-RE2 signals (impedance and overpotential) have been averaged.

4.2. Cr distribution in the Cr-exposed cathode throughout the layer thickness examined with SEM-WDX

The Cr distribution over the depth of the Cr-exposed WE was obtained with wavelength dispersive X-ray spectroscopy (WDX). Fig. 6A shows a backscattered electron (BSE) SEM image of the embedded and polished WE cross-section which was cut at 2 mm from the Cr source. An overlay of the Cr elemental mapping on the BSE image (Fig. 6B) demonstrates that Cr was not evenly spread throughout the cross-section of the WE. A considerable amount of Cr was accumulated in the region close to the LNF surface, whereas in the middle of the LNF cathode the concentration of Cr was lower. Close to the interface of LNF/GDC the amount of detected Cr was substantial. Cr accumulation within the 2 μm thick GDC layer was exceptionally high. The line profile of the relative Cr concentration throughout the LNF/GDC/YSZ assembly is presented in Fig. 6C.

The Ni SEM-WDX elemental map (not shown) indicates that Ni was detected everywhere in the LNF layer, as expected on basis of the LNF-composition. However, there were also a number of clearly visible spots with high Ni concentration indicating presence of Ni-rich metal oxide (also shown in Fig. 8).

Cr presence in the LNF layer together with Ni-rich precipitates confirms the Cr incorporation into the LNF perovskite as reported in

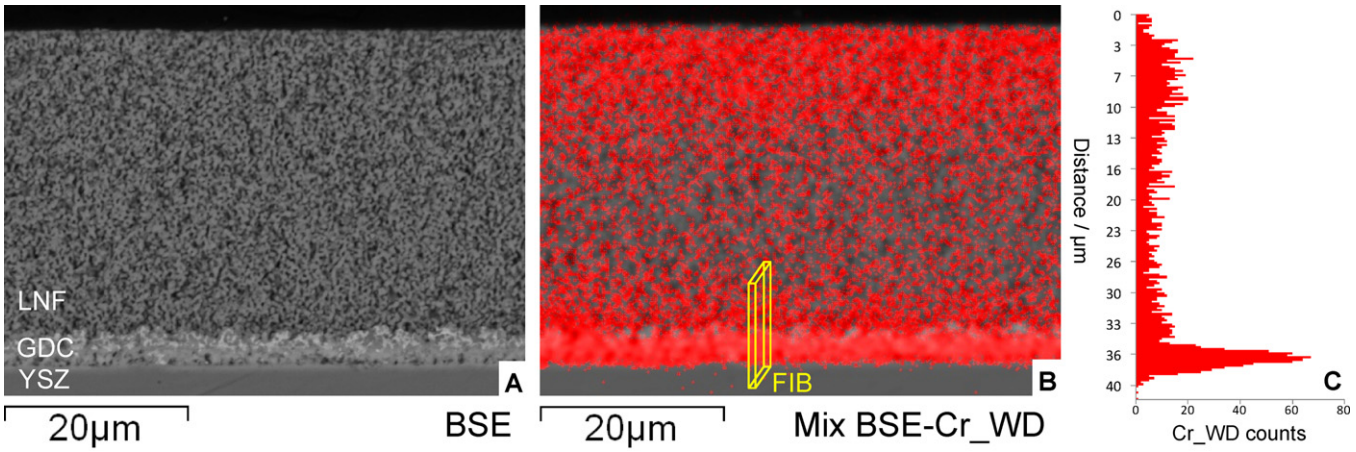

Fig. 6. Backscattered electron (BSE) SEM image of the embedded and polished WE cross-section taken 2 mm from the Cr source (A). In red (B) an overlay of the Cr elemental mapping on the BSE image. (C) A vertical line scan of the Cr counts. A yellow cuboid in (B) indicates schematically a location of the TEM specimen acquired using FIB. (For interpretation of the references to color in the figure caption, the reader is referred to the web version of the article.)

[11] which explains the observed in-plane electronic conductivity decrease. Furthermore, Cr presence at the LNF/GDC interface could be the cause for the increase in R_{pol} as well as in R_{ohmic}. However, there might also be a severe effect of Cr-incorporation in the GDC-layer on R_{pol} and R_{ohmic}. The Cr-incorporation in the GDC-layer is caused by a reaction of Cr-species with the GDC layer, as further explained in Section 4.3.2.

4.3. Cr distribution in the Cr-exposed cathode at the interface of LNF/GDC/YSZ examined with STEM-EDX

The origin of the TEM specimen is schematically shown by the yellow cuboid in Fig. 6B. The specimen was cut out by means of FIB lift-out sample preparation and is presented in Fig. 7A. The STEM/HAADF image of Fig. 7B shows the investigated areas of the LNF/GDC/YSZ assembly after the final thinning step down to electron transparency. In Fig. 7B area 0 indicates the region of the STEM-EDX elemental mapping. Within the indicated rectangular areas 1, 3 and 4 in Fig. 7B the STEM-EDX elemental analyses were conducted. In areas 2 and 5 the STEM-EDX line scan was performed.

Fig. 8 presents the STEM-EDX mapping of the LNF/GDC/YSZ interface recorded over area 0 as indicated in Fig. 7B. The La, Ni and Fe maps show the region of the LNF grains. The Ni map shows additionally a Ni-rich precipitate (most likely NiO) located between the LNF grains. The Cr map revealed that Cr was incorporated into the periphery of the LNF particles. Cr-enrichment is clearly indicated by high Cr counts and coincides with Ni-poor concentrations at the edges of the LNF grains. Furthermore, the Cr map demonstrates overall high Cr concentration within the GDC layer with locally even higher Cr intensities. Regions of a very high Cr

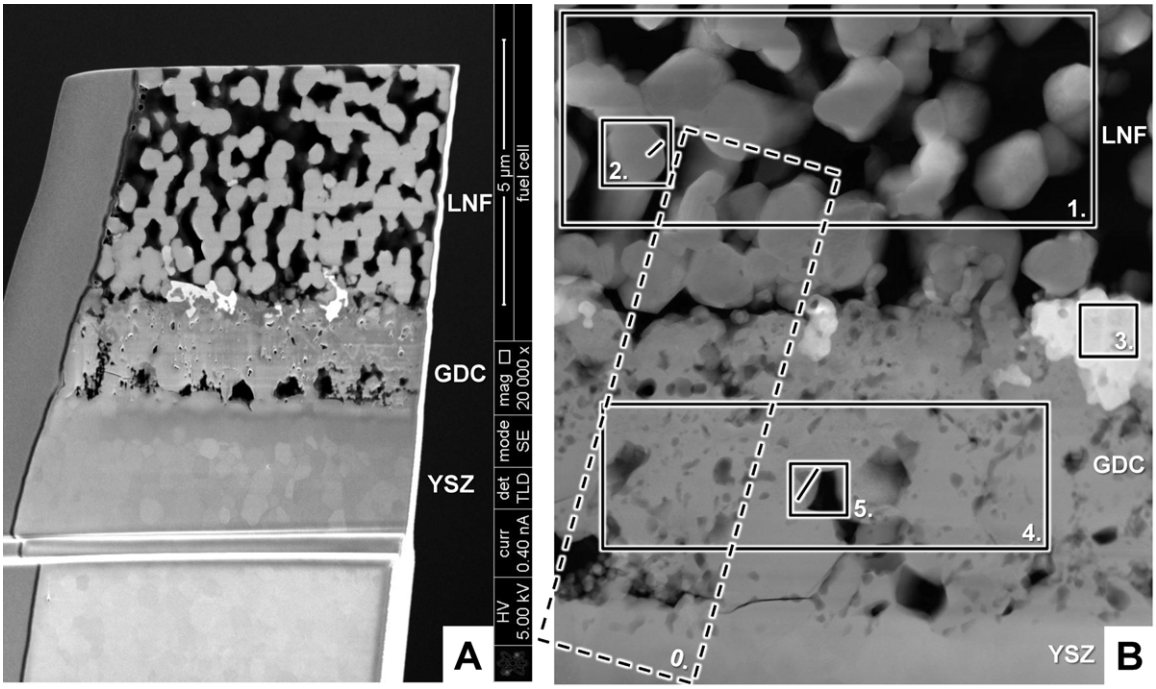

Fig. 7. FIB prepared TEM-specimen before the final thinning step (A) and STEM/HAADF image (B) indicating the investigated areas of interest across the LNF/GDC/YSZ assembly. Area 0 indicates the region of STEM-EDX mapping. Within areas 1, 3 and 4 STEM-EDX elemental analyses were conducted. In areas 2 and 5 STEM-EDX line scans was performed.

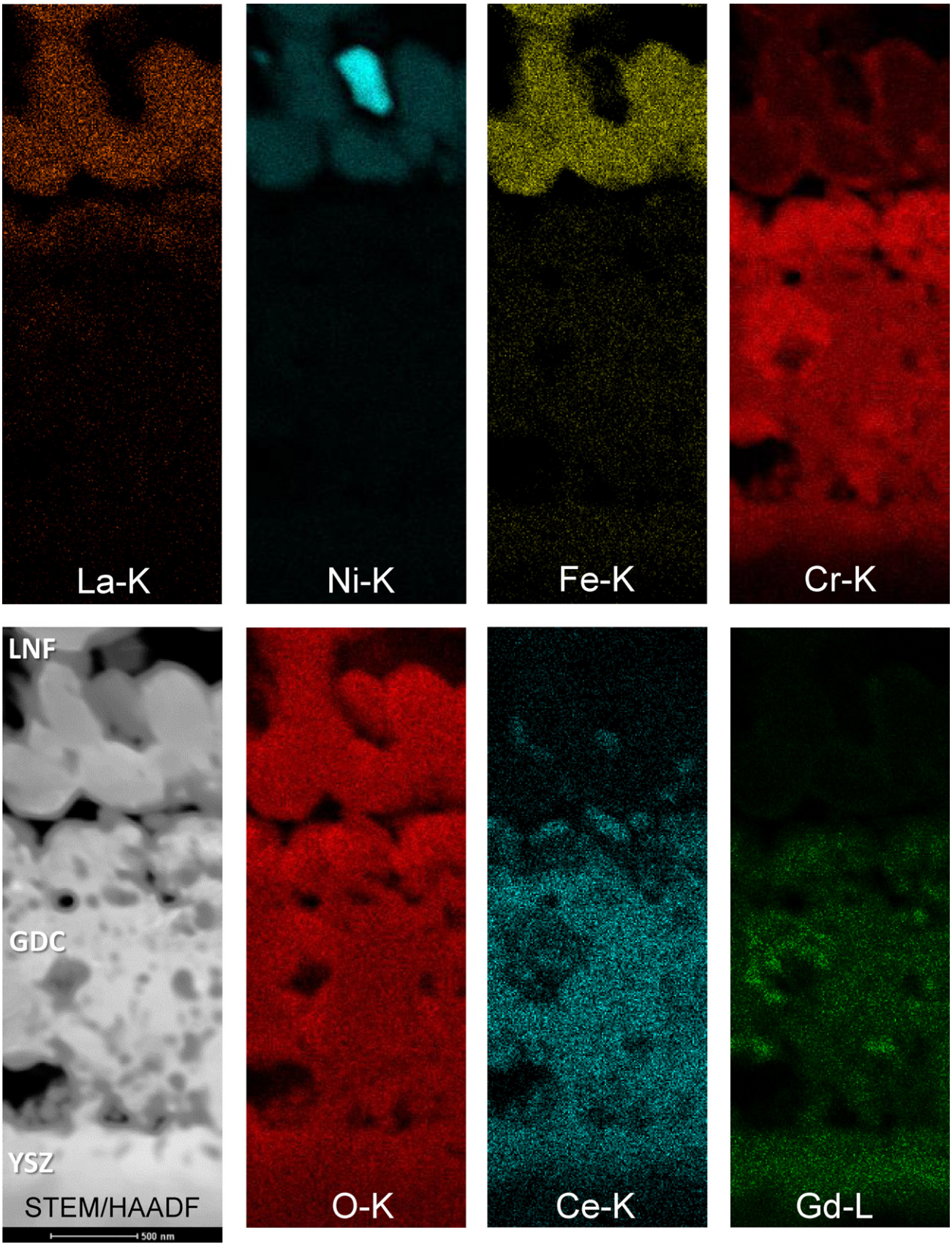

Fig. 8. STEM-EDX mapping of the LNF/GDC/YSZ interface presented on HAADF image. Raw count maps of La, Ni, Fe, Cr, O, Ce and Gd are shown over the 1.27 μm × 3.48 μm region (area 0 indicated in Fig. 7).

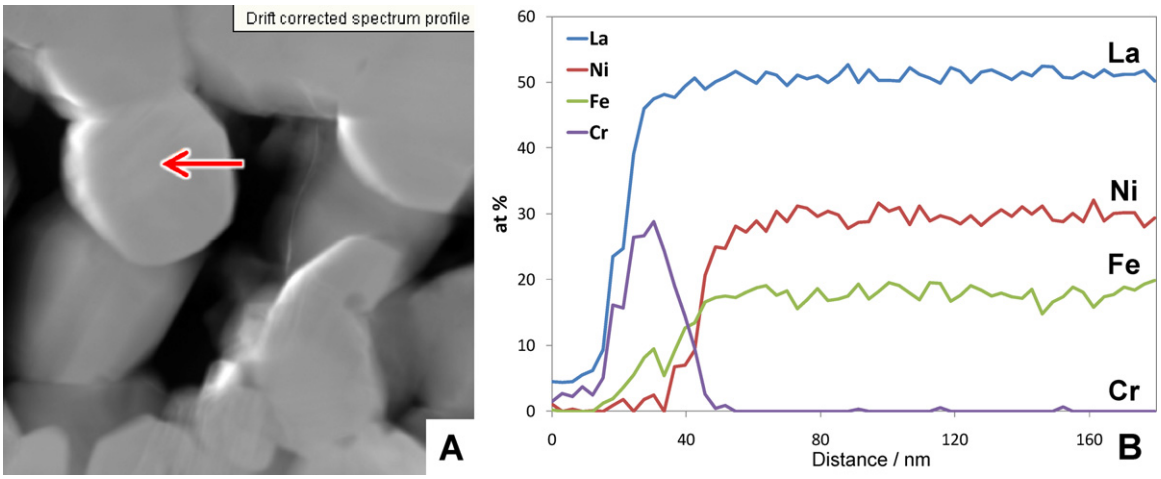

Fig. 9. HAADF image of the investigated LNF grain (A). The red arrow indicates position and direction of the STEM-EDX line scan which was performed at 60 equidistant points along the 180 nm long line. (B) The compositional profile (in atomic%) across the LNF grain. Close to the edge of the grain also the signal of carbon (originating from the epoxy) was taken into at.% calculations. (For interpretation of the references to color in the figure caption, the reader is referred to the web version of the article.)

concentration within the GDC layer overlap with Ce-poor and Gd-rich areas.

In Fig. 8 only raw count maps are presented, as the number of counts per pixel was too low to allow accurate quantification. Hence, further analysis by STEM-EDX was performed as indicated in Fig. 7B.

4.3.1. Cr distribution within the LNF layer

The STEM-EDX area scans within the LNF layer, indicated as area 1 in Fig. 7B, provided the following average elemental composition: 50.5 at.% of La, 29.2 at.% of Ni, 17.3 at.% of Fe and 3.0 at.% of Cr. This result confirms Cr accumulation of 3 at.% in the LNF layer close to the interface with GDC layer.

Fig. 9 presents the location of the STEM-EDX line scan across the LNF grain (performed in the area 2 in Fig. 7B). The compositional profile (in at.%) across the LNF grain indicated significant Cr enrichment in the outer shell of the LNF grain accompanied with a very low concentration of Ni together with lowered concentration of Fe. The Cr affected depth of the LNF grain was estimated to be up to ~30–40 nm. Such Cr penetration depth is in agreement with a TEM-EDX study, as described in an earlier paper by the authors [11]. In the middle of the grain the nominal LNF perovskite composition was preserved: La 50 at.%, Ni 30 at.%, Fe 20 at.%, as expected for $LaNi_{0.6}Fe_{0.4}O_3$.

Cr incorporation and Ni removal from the LNF perovskite justifies the decrease of the in-plane electronic conductivity as Cr-rich perovskite has lower electronic conductivity than Ni-rich [27]. The change in surface composition of the LNF-particles, especially close to the interface with the GDC-layer might be responsible for the increase in R_{pol}, as the cathode surface is known to play a significant role in the electrochemical process of oxygen reduction reaction (ORR) [28–30].

4.3.2. Cr distribution within the GDC layer

The STEM-EDX area scans within the GDC layer, indicated as area 4 in Fig. 7B, provided the following average composition: 47.1 at.% of Ce, 31.5 at.% of Gd and 21.4 at.% of Cr. The atomic ratio of Ce and Gd was 3:2 as in the nominal $Ce_{0.6}Gd_{0.4}O_{1.8}$. This finding revealed remarkably high Cr accumulation of more than 20 at.% in the GDC layer. An important fact is that such Cr-enrichment of GDC layer was not at all observed in the previous Cr-poisoning experiment [11], which was operated under conditions without current load, i.e. are comparable to OCV.

The STEM-EDX line scan was carried out as indicated in Fig. 10A and B by line 5b. The compositional profile (in at.%) across the investigated grains (Fig. 10C) shows Cr–Gd-rich grain across 300 nm distance and shift to a Ce–Gd-rich grain at the end of the scan.

Fig. 10A shows the location of the STEM-EDX area scans (area 5a in the middle of line 5b) performed on a distinctively different grain compared to a majority of GDC grains. The average composition obtained in the area 5a was: 4.9 at.% of Ce, 43.5 at.% of Gd and 51.6 at.% of Cr. Such composition suggested the presence of $GdCrO_3$ perovskite.

In order to investigate the crystal structure of a Cr–Gd-rich grain, in comparison with GDC grain, a HRTEM study was conducted in two regions as indicated in Fig. 10B.

The HRTEM image recorded on the edge of Cr–Gd-rich grain in the area 5a″ is shown in Fig. 10D. The fast Fourier transform (FFT) of the crystalline region (inset in Fig. 10D) revealed an electron diffraction pattern that could be indexed as belonging to an orthorhombic perovskite cell with the parameters: a_o = 5.3 Å, b_o = 5.5 Å, c_o = 7.6 Å, very close to the cell parameters of $GdCrO_3$ perovskite (ICDD 71-1275). The atomic composition obtained with STEM-EDX in area 5a may, therefore, be presented as $(Gd_{0.9}Ce_{0.1})CrO_3$.

The HRTEM image recorded on the edge of Ce and Gd rich grain in the area 5c″ is shown in Fig. 10E. The FFT of the crystalline region (inset in Fig. 10E) showed an electron diffraction pattern that could be indexed as belonging to a cubic fluorite cell with an a_o parameter of 5.4 Å, similarly to the cell parameters of $Gd_{0.30}Ce_{0.70}O_{1.85}$ fluorite (ICDD 75-0163). The atomic composition obtained with STEM-EDX in the end region of the line scan (Fig. 10C) may be thus presented as $Ce_{0.7}Gd_{0.3}O_x$.

STEM-EDX and HRTEM study of the Cr-exposed GDC layer revealed the presence of perovskite type Gd–Cr-rich grains located next to Ce-enriched fluorite GDC grains. Such impact of Cr on the GDC-layer phase composition has serious implications for the ionic conductivity of GDC layer and can therefore justify the observed increase in R_{ohmic} of the WE.

4.3.3. Pt deposits

The STEM-EDX area scans at the interface of LNF/GDC layer, indicated as area 3 in Fig. 7B, revealed the presence of a nearly pure Pt deposit. This finding suggests possible Pt evaporation from the Pt mesh after prolonged operation. In the reference sample (Cr-free 500 h at 800 °C under 400 mA cm^{-2}) the presence of Pt deposits was also detected (not shown here).

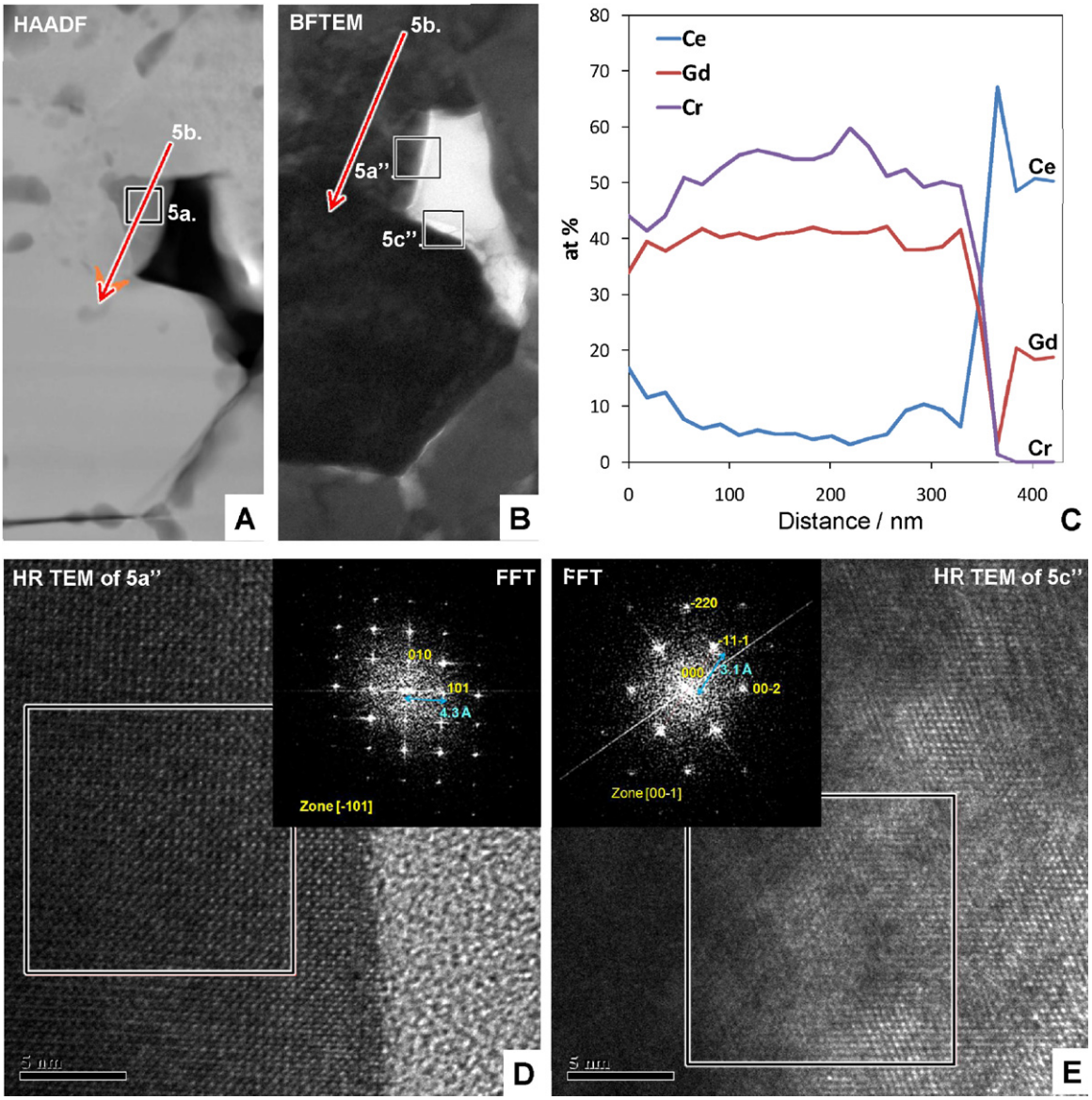

Fig. 10. HAADF (A) and BF-TEM image (B) of the Cr-GDC grains. A red arrow indicates the position and direction of the STEM-EDX line scan of 420 nm with EDX taken every 17.5 nm. (C) Resulting at.% compositional profile. (D) and (E) HRTEM images of the positions in (B) with a corresponding FFT (as the insets). (For interpretation of the references to color in the figure caption, the reader is referred to the web version of the article.)

5. Mechanism of Cr-poisoning – discussion

The LNF cathode tested in a Cr-free atmosphere showed no apparent degradation with stable values of both R_{ohmic} and R_{pol}, confirming the intrinsic electrochemical stability of the LNF cathode under operating conditions.

However, the LNF cathode tested in combination with the Cr-source showed clear deterioration of both R_{ohmic} and R_{pol}, indicating extrinsic degradation due to volatile Cr-species, which entered the working electrode (WE) and affected both the LNF cathode layer and the GDC barrier layer.

The top of the LNF cathode is assumed to be electrochemically inactive, serving just as a current collector. The presence of Cr in the top layer indicates that a chemical reaction of volatile Cr-species took place in this part of the LNF perovskite layer, which is in accordance with the Cr exposure study at open circuit voltage (OCV) [11]. The observed loss of the in-plane electronic conductivity of the LNF layer, which was due to Cr-incorporation, contributed only partly to the increase in R_{ohmic}. The middle part of the LNF layer has been less affected by Cr, showing a relatively 'low-Cr-accumulation zone'. This is not in accordance with the findings under OCV conditions [11], where the Cr-distribution was uniform over the whole LNF-layer thickness. The lower Cr-content in the middle part of the LNF layer is most likely a consequence of the electrochemical driving force for Cr accumulation towards the LNF/GDC interface. This is clearly demonstrated by high Cr concentration detected within a few microns from the LNF/GDC interface. In this region the electrochemically driven reaction is assumed to be even more significant than the chemical reaction. The more reducing conditions at the LNF/GDC interface [30,31] is very likely to reduce the gaseous Cr^{VI}-species [32,33] to Cr^{III} which was directly exchanged with Ni in the LNF lattice. Such a change in the surface composition of the LNF-particles, into La–Cr-rich perovskite, might be responsible for the deterioration of the electrochemical activity for the oxygen reduction reaction (ORR) and thus contributing to the increase of R_{pol}. Cr incorporation into the LNF grains, up to tens of nm, was accompanied by a segregation of NiO-precipitates throughout the LNF layer thickness in accordance with a previous study at OCV [11].

A massive Cr deposition of more than 20 at.% was observed within the 2 μm thick GDC layer. Cr reacted with Gd to form a $GdCrO_3$ perovskite. The $GdCrO_3$ layer might impede transport of oxygen ions from triple phase boundaries (TPB) to YSZ electrolyte, as this perovskite has significantly lower ionic conductivity compared to fluorite GDC [34,35]. In the periphery of the GDC grains, the detected composition of $Ce_{0.7}Gd_{0.3}O_x$ might exhibit locally higher ionic conductivity compared to nominal $Ce_{0.6}Gd_{0.4}O_{1.8}$ [34]. Such a local improvement of ionic conductivity would be negligible considering the fact that GDC grains were covered and surrounded by the poorly conducting $GdCrO_3$ particles. Cr deposition within the GDC layer, taking place under current loading, is clearly in contrast with the absence of Cr deposition observed within the GDC layer during OCV test [11]. Under the electrochemical operation the local oxygen partial pressure within GDC layer is estimated to be in the range of 10^{-8}–10^{-10} atm. Lower partial pressure of oxygen combined with electrochemically enhanced reaction might explain the observed massive Cr deposition within GDC layer. Concluding, it seems that the blocking effect for the ionic transport caused by Cr-rich particles within GDC layer contributed to the increase of R_{ohmic}.

To the best knowledge of the authors, the present study reports, for the first time in the literature, that Cr-poisoning affected not only the cathode material (LNF) but also the barrier layer (GDC).

The electrochemical reaction mechanism for the reduction of oxygen by the LNF cathode is probably restricted mainly to the TPB region (similarly to LSM), as suggested by the (minor) deposition of Pt at the interfaces and a very low bulk ionic conductivity of LNF [1,36,37]. Therefore, the oxygen reduction reaction (ORR) is localized and restricted to the TPB, unlike for the LSCF cathode (which is a MIEC cathode, hence its comparatively high bulk ionic conductivity broadens the ORR region [38,39]). An ORR region severely limited to the TPB will most likely cause a steep gradient in pO_2 near or at the LNF/GDC interface (local drop in pO_2) which could enhance Cr deposition and subsequent reaction with GDC. This is clearly in contrast with measurements at OCV [11], where no reaction of Cr-species with GDC was observed. The observed massive Cr-deposition in the doped ceria layer, compared with the LNF cathode layer, suggests indeed that the electrode reaction model is restricted to the TPB and that volatile Cr-species can easily reach the TPB area, similar to what has been observed for the LSM cathodes [6].

The different chemical nature of LNF, as compared to LSM or LSCF, in terms of the absence of the Cr-nucleating-agents [5] (like Mn^{2+} and/or SrO [5–7]) is resulting in a different Cr-poisoning behavior. The main characteristic feature of LNF as cathode material is that it does not contain Sr, hence no formation of $SrCrO_4$ occurs, which has been reported frequently for the Cr-poisoning of LSCF cathodes [5,7]. It seems therefore that the lower LNF-reactivity with Cr-species allows the Cr-containing vapors to reach to the TPB areas and react further with the GDC barrier layer. Cr reactivity with the GDC layer has so far not been reported for GDC/LSCF cathodes.

The present study should be regarded as an accelerated Cr-poisoning test (owing to a porous Fe–Cr interconnect foam with a high Cr-release rate) allowing for the insight into the Cr-poisoning mechanism after relatively short testing period. However, a comparative study, in practical and reproducible IT-SOFC stack conditions, with other SOFC cathodes is needed to provide a realistic Cr-tolerance evaluation.

A composite LNF:GDC interlayer (with low Gd content) might be an interesting research direction for increasing and spreading the TBP region thus avoiding a localized high overpotential zone (with locally very low pO_2) hence possibly significantly reducing Cr-poisoning impact on the Sr- and Mn-free LNF cathode material.

6. Conclusions

The absence of degradation for the $LaNi_{0.6}Fe_{0.4}O_3$ (LNF) cathode, when tested in Cr-free atmospheres, confirmed the intrinsic electrochemical stability of LNF. However, extrinsic degradation, due to volatile Cr-species, caused LNF cathode performance loss.

Based on the presented observations the following mechanism has been derived for Cr-poisoning of $LaNi_{0.6}Fe_{0.4}O_3$ cathodes under current load:

(1) Overpotential and impedance increase was due to reaction of volatile Cr-species with both LNF grains and the GDC barrier layer.
(2) R_{ohmic} increase was caused by a decrease of the in-plane electronic conductivity of the LNF layer, due to Cr incorporation and Ni removal from LNF, and a deterioration of the ionic conductivity of the GDC layer, due to formation of a $GdCrO_3$ phase.
(3) R_{pol} increase was caused by a decrease of electrochemical activity of the LNF surface towards oxygen reduction reaction at the TPB, due to Cr presence in the outer shell of the LNF grains.
(4) Chemical reaction and electrochemically driven reaction of volatile Cr-species with LNF and GDC contributed to degradation of LNF cathodes under current load.

Acknowledgements

This work was partly supported by the European Commission, as part of the European Project SOFC600 (SES6-CT-2006-020089), and partly supported by funding from ECN. Wim Haije and Paul Cobden are thanked for discussions and comments. Sebastian Molin is acknowledged for performing the van der Pauw measurements and useful discussions. ECN Engineering & Services (Materials Testing & Consultancy group) is thanked for the SEM and ICP-OES analysis. ECN Engineering & Services (MT&C and Realisation) is acknowledged for development of the laser trimming process and various laser cutting assistance. Philips Innovation Services (MiPlaza) is acknowledged for materials analysis. Especially, Carlo Manders is thanked for the SEM-WDX measurements and Marcel Verheijen is gratefully acknowledged for the STEM analyses.

References

[1] R. Chiba, F. Yoshimura, Y. Sakurai, Solid State Ion. 124 (1999) 281.
[2] T. Komatsu, H. Arai, R. Chiba, K. Nozawa, M. Arakawa, K. Sato, Electrochem. Solid-State Lett. 9 (2006) A9J.
[3] Y.D. Zhen, A.I.Y. Tok, S.P. Jiang, F.Y.C. Boey, J. Power Sources 170 (2007) 61.
[4] G.Y. Laua, M.C. Tucker, C.P. Jacobson, S.J. Visco, S.H. Gleixner, L.C. DeJonghe, J. Power Sources 195 (2010) 7540.
[5] S.P. Jiang, Y.D. Zhen, Solid State Ion. 179 (2008) 1459.
[6] S.P. Jiang, J.P. Zhang, X.G. Zheng, J. Eur. Ceram. Soc. 22 (2002) 361–373.
[7] S.P. Jiang, S. Zhang, Y.D. Zhen, J. Electrochem. Soc. 153 (2006) A127.
[8] M. Stodolny, F.P.F. van Berkel, B.A. Boukamp, ECS Trans. 25 (2) (2009) 2915–2922.
[9] M.K. Stodolny, B.A. Boukamp, D.H.A. Blank, F.P.F. van Berkel, J. Electrochem. Soc. 158 (2) (2011) B112–B116.
[10] M. Stodolny, F.P.F. van Berkel, B.A. Boukamp, ECS Trans. 35 (1) (2011) 2035–2043.
[11] M.K. Stodolny, B.A. Boukamp, D.H.A. Blank, F.P.F. van Berkel, J. Power Sources 196 (2011) 9290–9298.
[12] M. Nagata, Y. Itoh, H. Iwahara, Solid State Ion. 67 (1994) 215.
[13] F.P.F van Berkel, F.H. van Heuveln, J.P.P. Huijamans, Solid State Ion. 72 (1994) 240.
[14] S.B. Adler, J. Electrochem. Soc. 149 (2002) E166.
[15] J. Rutman, I. Riess, Electrochim. Acta 52 (2007) 6073–6083.
[16] E. Ivers-Tiffée, A. Weber, K. Schmid, V. Krebs, Solid State Ion. 174 (2004) 223–232.
[17] J. Winkler, P.V. Hendriksen, N. Bonanos, M. Mogensen, J. Electrochem. Soc. 145 (1998) 1184.
[18] B.A. Boukamp, Solid State Ion. 20 (1) (1986) 31–44.
[19] B.A. Boukamp, Solid State Ion. 18–19 (1986) 136.
[20] B.A. Boukamp, Equivalent Circuit (Version 1.2), Copyright, University of Twente/WisseQ, 1985–2009.
[21] B.A. Boukamp, D.H.A. Blank, IEEE-TUFFC 58 (12) (2011) 2521–2530.

[22] W. Glatz, G. Kunschert, M. Janousek, in: M. Mogensen (Ed.), Proc. 6th European Solid Oxide Fuel Cell Forum, European Fuel Cell Forum, Switzerland, 2004.
[23] W. Glatz, G. Kunschert, et al., Electrochemical Society Proceedings, Vol. 1, 2005-07, pp. 1773/1780, 9th International Symposium on Solid Oxide Fuel Cells, Quebec City, Canada, 2005, ISBN 1-56677-466-7.
[24] R. Chiba, Y. Tabata, T. Komatsu, H. Orui, K. Nozawa, M. Arakawa, H. Arai, Solid State Ion. 178 (2008) 1701–1709.
[25] S.P.S. Badwal, R. Deller, K. Foger, Y. Ramprakash, J.P. Zhang, Solid State Ion. 99 (1997) 297.
[26] Y. Matsuzaki, I. Yasuda, Solid State Ion. 132 (2000) 271–278.
[27] H.E. Höfer, R. Schmidberger, J. Electrochem. Soc. 141 (1994) 782.
[28] S.B. Adler, J.A. Lane, B.C.H. Steele, J. Electrochem. Soc. 143 (11) (1996) 3554–3564.
[29] F.H. van Heuveln, H.J.M. Bouwmeester, J. Electrochem. Soc. 144 (1) (1997) 135–140.
[30] Y. Li, R. Gemmena, X. Liu, J. Power Sources 195 (2010) 3345–3358.
[31] S.P. Jiang, J. Mater. Sci. 43 (2008) 6799–6833.
[32] M.C. Tucker, H. Kurokawa, C.P. Jacobson, L.C. De Jonghe, S.J. Visco, J. Power Sources 160 (2006) 130.
[33] K. Hilpert, D. Das, M. Miller, D.H. Peck, R. Weiss, J. Electrochem. Soc. 143 (1996) 3642.
[34] Z. Tianshu, P. Hing, H. Huang, J. Kilner, Solid State Ion. 148 (2002) 567–573.
[35] V.V. Kharton, A.A. Yaremchenko, E.N. Naumovich, J. Solid State Electrochem. 3 (6) (1998) 303–326, doi:10.1007/s100080050161.
[36] M. Gazda, P. Jasinski, B. Kusz, B. Bochentyn, K. Gdula-Kasica, T. Lendze, W. Lewandowska-Iwaniak, A. Mielewczyk-Gryn, S. Molin, Solid State Phenom. 183 (2011) 65.
[37] J.Y. Chen, J. Rebello, V. Vashook, D.M. Trots, S.R. Wang, T.L. Wen, J. Zosel, U. Guth, Solid State Ion. 192 (1) (2011) 424–430.
[38] J. Molenda, K. Świerczek, W. Zając, J. Power Sources 173 (2007) 657–670.
[39] A. Weber, E. Ivers-Tiffée, J. Power Sources 127 (2004) 273–283.